Hindawi
Advances in Civil Engineering
Volume 2020, Article ID 8886402, 12 pages
https://doi.org/10.1155/2020/8886402

Research Article

Monitoring System for Circular Deformation in Metro Shield Tunnels in Soft Soils

Jinfeng Zhang and Ming Zhao

Department of Civil Engineering, Tongji University, 1239 Siping Road, Shanghai 200092, China

Correspondence should be addressed to Ming Zhao; zhaom@tongji.edu.cn

Received 7 July 2020; Revised 16 August 2020; Accepted 17 August 2020; Published 1 September 2020

Academic Editor: Valeria Vignali

For in-service metro shield tunnels in soft soils, large circular deformations are a major concern because they usually lead to various problems, such as water leakage, joint openings, and concrete cracks. However, the monitoring of circular deformation depends mainly on manual surveying, and the automatic monitoring methods developed in recent years generally have low economic applicability and are not widely implemented. In this study, an automatic and cost-effective system was presented to monitor circular deformation in shield tunnels by using only inclinometers. Experiments were conducted to prove the assumption that each segment can be regarded as a rigid body and to investigate the position of the joint rotation center. Then, a method for monitoring circular deformation based on the rigid body and plane section assumptions was proposed. The joint opening angle, maximum joint opening width, horizontal diameter convergence, and bolt strain were calculated from rotation angles of segments which can be monitored directly by inclinometer. A case study was conducted for a section of a metro shield tunnel with an ongoing pit excavation nearby. The rotation of segments was measured using MEMS inclinometers, and the data were transmitted using ZigBee and general packet radio service (GPRS) wireless communication technology. Results show that the proposed system could be implemented to improve transportation safety in relevant situations and similar conditions.

1. Introduction

Among various subway tunnel construction methods, shield-driven tunneling has been widely adopted in soft soils owing to its flexibility, cost-effectiveness, high speed, and small disturbance to the ground surface [1–3]. A shield tunnel is an assembled structure comprising several precast reinforced concrete segments and segmental joints, and, consequently, the reaction of the ground is critical to the stability of the system [4–6]. However, there exist many problems with this method such as leakage, concrete cracking and spalling, steel corrosion, and sliding and opening deformation of lining joints, and the occurrence of these conditions worsens with metro operation [7, 8]. Almost all of these issues are interrelated and are linked to the tunnel structure deformation [9]. Generally speaking, the causes of tunnel deformation mainly include earth pressure due to geological factors, the deterioration of the lining materials, water leakage and frost damage, and newly constructed adjacent buildings [10–12]. In addition, as metro tunnels generally have a shallow depth and are constructed in soft soils, large tunnel deformations may trigger ground settlement and cause damage to the surface structures [13, 14].

To eliminate the inefficiency and lag of traditional manual monitoring methods, much research has been devoted to the monitoring of tunnel structures: a hybrid wireless sensor network has been developed to monitor the lining deformation in London [15]; a strain-monitoring system using Brillouin optical time-domain reflectometry technology has been set up to monitor joint movements in a tunnel lining [16]; and a settlement and lateral displacement monitoring method for a shield tunnel based on an improved conjugated beam method using distributed fiber optic sensors has been proposed [17]. In addition, the monitoring of uneven settlement, segment dislocation

deformation, cracks, and leakage has also been studied [18–22]. However, most existing or established monitoring methods/systems have failed to achieve both automatic and economic goals. A high degree of automation and low cost are key for achieving the wide implementation of a monitoring system in the large-scale underground transportation system.

Studies of monitoring methods for the circular deformation of a shield tunnel lining have mainly focused on calculating the horizontal diameter convergence, and the rotation center of the joint has been assumed to be located at the end of the compressive zone [23] or at the center of the joint section [24]. In this study, based on experimental verification of the rigid body hypothesis and the position of the joint rotation center, a monitoring method was proposed to obtain the circular deformation by measuring the rotation angles of segments, thus requiring only inclinometers. The correction of monitoring data and an early warning strategy were also presented in detail. Finally, a case study was described, in which the monitoring method was applied to develop a monitoring system. From the perspective of long-term monitoring, the cost of inclinometers is lower than that of manual monitoring or other large-scale automatic monitoring instruments, such as intelligent total station network monitoring systems, prism-free automatic tracking total station monitoring, and electric levels.

2. Experimental Study

2.1. Test Setup and Loading Scheme. To investigate the behavior of the longitudinal joint under a positive bending moment (PBM, joint opens inwards) and a negative bending moment (NBM, joint opens outwards), six groups of PBM tests (PBM-1–PBM-6) and six groups of NBM tests (NBM-1–NBM-6) were conducted using the setup shown in Figure 1. The test specimens were taken from the lining ring of Shanghai metro shield tunnels and were composed of an adjacent block and a standard block after cutting.

All tests were conducted with the 2000 kN loading frame in the Laboratory of Building Structures in Tongji University. One end of the specimen was connected to a fixed hinge support and the other end to a sliding hinge support. Connected with ground anchors, the members under the two hinge supports comprised the specimen's support system. Downward loads were applied to the segments first through the transverse beam and then through the longitudinal beams welded with steel rods. In addition, a steel plate with a thickness of 20 mm was placed between the steel rod and the specimen to avoid local concrete failure. A horizontal load was applied to the sliding hinge support to produce an NBM. The reaction forces of the jacks were borne by the counterforce frame.

The PBM loading scheme was as follows: the horizontal force N and vertical force F were simultaneously applied from 0. N was increased to 200 kN for four groups (PBM-1–PBM-4) and 440 kN for two groups (PBM-5–PBM-6) and then remained unchanged; F was initially loaded by force and then by displacement after the bolts yielded until the specimen failed.

The NBM condition was such that F was increased from 0 to 60 kN in groups NBM-1–NBM-4 and 80 kN in groups NBM-5–NBM-6, following which it remained the same. N was initially loaded by force from 0 and then by displacement after the bolts yielded until the specimen failed.

2.2. Measurement Items. The deformation or displacement of the specimen in the experiment was reported with the following measurements: joint opening, mid-span deflection, support displacement, and rotation of segments, as shown in Figure 2. The joint opening and closing were measured by displacement meters around the joint position, which were numbered Δ1–Δ3 on the specimen's inner surface and Δ4–Δ6 on the outer surface. Eight inclinometers were used to monitor the rotation angle of two segments ($\varphi_1 - \varphi_8$).

2.3. Test Results. If the segmental rotation is a rigid body rotation, the joint opening angle would be equal to the sum of the rotation angles of the segments on both sides of the joint. Figure 3 illustrates the relationship between the joint opening angle and the bending moment, in which the joint opening angle was calculated by two methods. One method sums the rotation angles of the two segments, and the other calculates the angle using the following equation:

$$\theta = \frac{\Delta_{\text{opening}} + \Delta_{\text{closure}}}{h}, \tag{1}$$

where θ is the joint opening angle (rad); Δ_{opening} is the opening value of the joint measured by Δ_1, Δ_2, and Δ_3 under PBM and by Δ_4, Δ_5, and Δ_6 under NBM (mm); Δ_{closure} is the closure value of the joint, measured by Δ_4, Δ_5, and Δ_6 under PBM and by Δ_1, Δ_2, and Δ_3 under NBM (mm); and h is the height of the joint section (mm).

As shown in Figure 3, the results of the two methods were consistent, with only slight differences at the later stage of loading, thus proving the rigid body assumption for segments. The reasons for the differences mainly include the following: (1) the segment itself is slightly deformed during loading, especially near the area of the joint; (2) after cutting, the end of the segment cannot be guaranteed to be a right angle, which affects the overall deformation; and (3) the accuracy of the displacement meters for measuring the segment opening and closing is lower than that of the inclinometers.

The relationship between the compression height of the joint section and the bending moment is shown in Figure 4. The compression height mainly varied from 75 to 150 mm with the applied PBM, which is equivalent to 21% to 43% of the segment thickness (350 mm). Meanwhile, under NBM, the compression height mainly varied from 57 mm to 85 mm, which is equivalent to 16% to 24% of the segment thickness. Obviously, there is a certain distance between the joint rotation center and the edge of the compressive zone when it is not under full section compression. Therefore, based on the test results, it is recommended that the distance

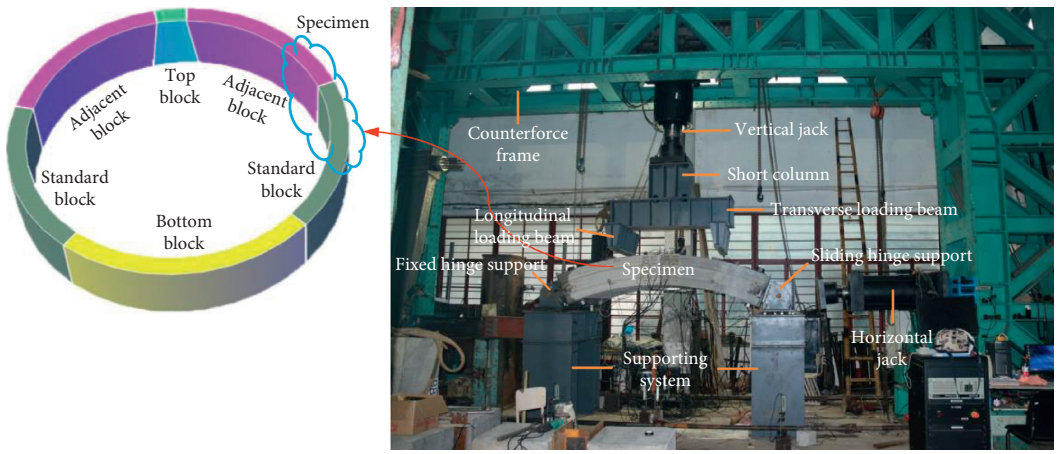

Figure 1: Experimental setup and specimen. The specimen had a central angle of approximately 46°. Two high-strength bolts were used to connect the two segments.

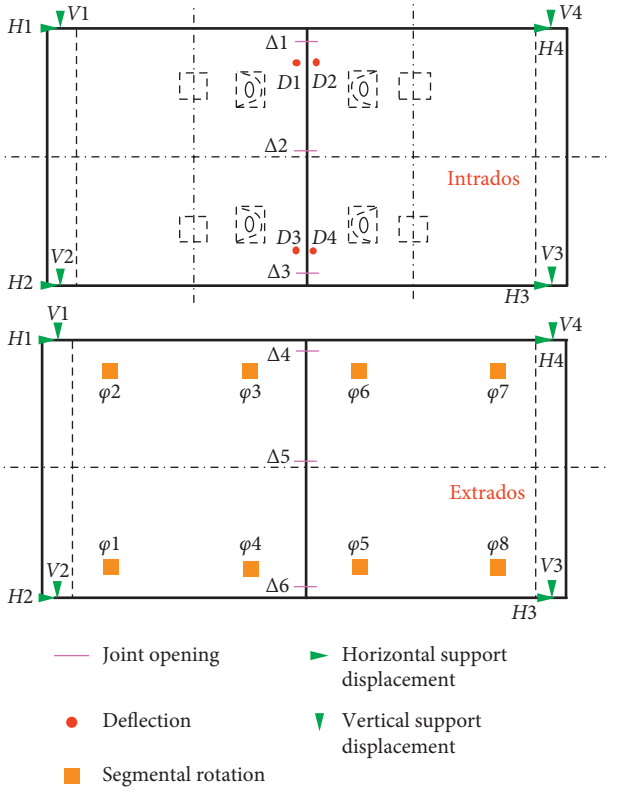

Figure 2: Layout of displacement meters and inclinometers.

between the joint rotation center and compressive edge is 115 mm under PBM and 75 mm under NBM.

Once the opening direction of the joint is determined, the position of the joint rotation center can be determined according to the recommended value. In general, the method to determine the joint rotation position is as follows: monitor the segment rotation direction ⟶ determine the joint opening direction ⟶ obtain the joint rotation position. Using this method, the joint rotation position was determined to be 115 mm away from the edge of the compressive zone when opening inwards and 75 mm when opening outwards.

3. Monitoring Method

As shown in Figure 5, there are six segments and six joints in a typical lining ring of the Shanghai metro shield tunnel. The segments include one top block (TF) with an average central angle of 16°, two adjacent blocks (TL1 and TL2) and two standard blocks (TB1 and TB2) with average central angles of 65°, and one bottom block (TD) with a central angle of 84°. The ring has an outer diameter of 6.2 m, inner diameter of 5.5 m, segmental thickness of 0.35 m, and length of 1.2 m.

The following assumptions were made in the derivation of the monitoring method:

(1) Segments are rigid bodies, as has been proved experimentally. In other words, the segmental rotation is mainly the rigid body rotation.

(2) The bottom block is static during the deformation; that is, the displacement of other segments is relative to the bottom segment.

(3) The joint section conforms to the assumption of plane section, which relates to the characteristics of concrete members.

From assumption (1), the opening angle of each joint is equal to the sum of the rotation angles of segments on both sides of the joint.

3.1. Maximum Joint Opening Width. According to the aforementioned assumptions, the deformation mode of a joint section under PBM and NBM can be described as shown in Figure 6. The following equation can be obtained from the geometric relationship:

$$\tan\left(\frac{\theta}{2}\right) = \frac{(\Delta/2)}{h-y}. \tag{2}$$

Then,

$$\Delta = 2(h-y)\tan\left(\frac{\theta}{2}\right) \approx 2(h-y)\cdot\left(\frac{\theta}{2}\right) = (h-y)\theta, \tag{3}$$

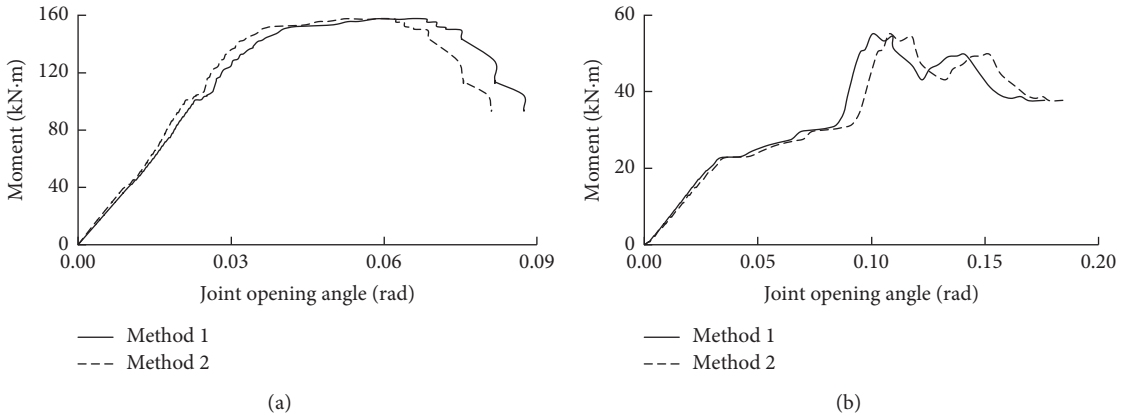

Figure 3: Relationship between joint opening angle and moment under (a) PBM, group PBM-6, and (b) NBM, group NBM-6. Method 1 in the legend represents the sum of the rotation angles of the two adjacent segments. Method 2 represents the joint opening angle calculated by Equation (1).

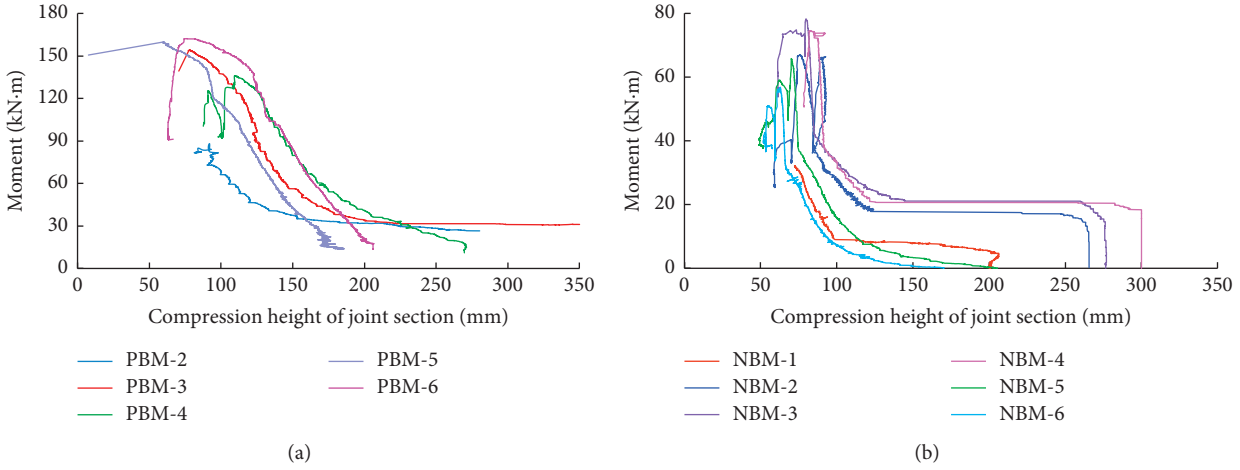

Figure 4: Relationship between compression height of joint section and moment under (a) PBM and (b) NBM. Each curve represents the test results of one test group.

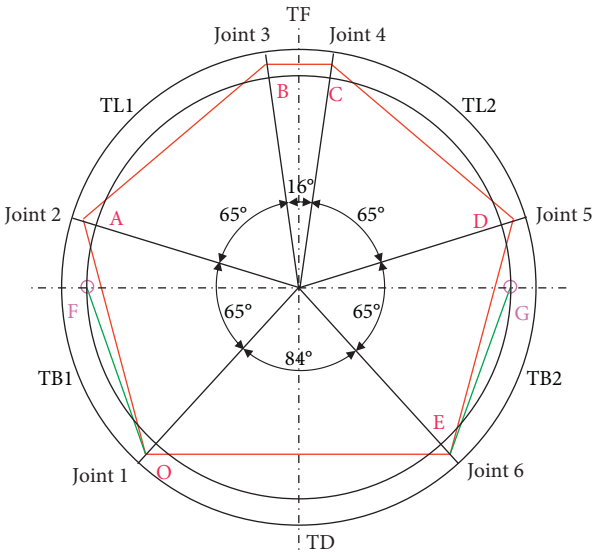

Figure 5: Lining ring of Shanghai metro shield tunnel. Points F and G are the measuring points of horizontal diameter convergence. Points O, A, B, C, D, and E are the rotation centers of each joint, not the middle points of the joints.

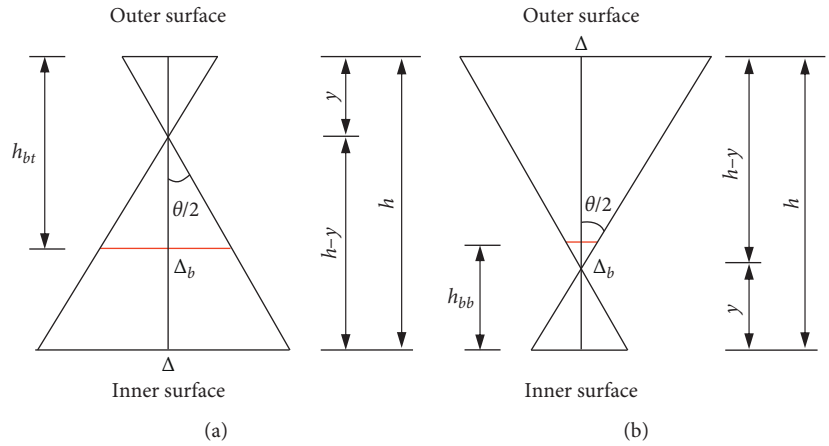

Figure 6: Relationship of joint opening angle and maximum opening value for (a) PBM and (b) NBM.

where Δ is the maximum joint opening width (mm); and y is the compression height of the joint section (mm).

3.2. Horizontal Diameter Convergence. As the bottom block is assumed to be still when the lining ring is deformed, according to the geometric diagram shown in Figure 7, the convergence of the horizontal diameter is approximately equal to the horizontal coordinate increment of the measuring points F and G, owing to the small rotation angle of the segment.

Taking the calculation of ΔD_2 as an example, when TB2 rotates φ_4 clockwise, the convergence value of the horizontal diameter is

$$\Delta D_2 = l_{EG}\cos\alpha_4 - l_{EG}\cos(\alpha_4 - \varphi_4) = l_{EG}\cos\alpha_4 - l_{EG}\cos\alpha_4\cos\varphi_4 + l_{EG}\sin\alpha_4\sin\varphi_4. \quad (4)$$

As the segmental rotation angle is small, $\sin\varphi \approx \varphi$ and $\cos\varphi \approx 1 - \varphi^2/2$; this gives

$$\Delta D_2 = l_{EG}\cos\alpha_4 - l_{EG}\left(1 - \frac{\varphi_4^2}{2}\right)\cos\alpha_4 + l_{EG}\varphi_4\sin\alpha_4 \approx l_{EG}\varphi_4\sin\alpha_4. \quad (5)$$

Assuming that the angle is positive when the segment rotates counterclockwise, the horizontal diameter convergence generated by the two standard blocks' rotation can be expressed as

$$\Delta D = l_{OF}\varphi_1\sin\alpha_1 - l_{EG}\varphi_4\sin\alpha_4, \quad (6)$$

where φ_1 and φ_4 correspond to the rotations of TB1 and TB2 (rad), respectively; l_{OF} (l_{EG}) refers to the distance between the measuring point F (G) and the rotation center O (E) at joint 1 (joint 6) (mm); and α_1 (α_4) is the initial angle between l_{OF} (l_{EG}) and the horizontal line (rad).

3.3. Bolt Strain. The elongation of the bolt can be derived from the joint opening angle and the joint compression height. According to the geometric relationship shown in Figure 6, when a joint opens inwards (PBM condition),

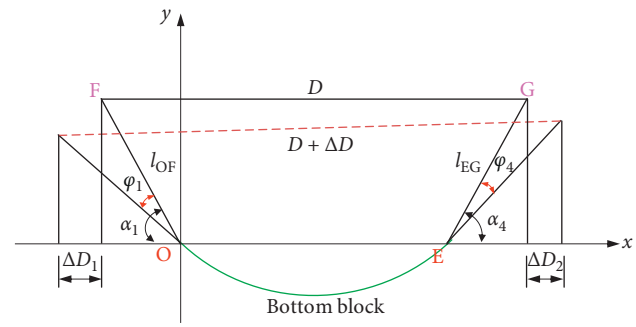

Figure 7: Geometric relationship between horizontal diameter convergence and segment rotation. Points F and G are the measuring points of horizontal diameter convergence.

$$\Delta_b = \theta(h_{bt} - y), \quad (7)$$

and when a joint opens outwards (NBM condition),

$$\Delta_b = \theta(h_{bb} - y), \quad (8)$$

where Δ_b is the elongation of the bolt (mm), and h_{bt} and h_{bb} are the height from the bolt center to the compressive edge when the joint opens inwards and outwards, respectively.

Then, the bolt strain can be calculated as

$$\varepsilon_b = \frac{\Delta_b}{l_b}, \quad (9)$$

where ε_b is the bolt strain (mm) and l_b is the length of the bolt (485 mm).

Furthermore, the bolt stress in the elastic stage can be obtained as

$$\sigma_b = E_b\varepsilon_b, \quad (10)$$

where σ_b is the bolt stress (mm) and E_b is the elastic modulus of the bolt (1.8×10^5 MPa).

3.4. Correction of Monitoring Data. Under the previous assumptions, the number of degrees of freedom of the lining ring is reduced to four; therefore, the whole deformation of

the lining ring can be determined by measuring the rotation of the two adjacent blocks and the two standard blocks. Owing to the measurement error and assumptions of the calculation model, it is necessary to correct the monitoring data.

In the correction process, the initially included angles between TB1, TL1, TL2, and TB2 and the X-axis forward direction were set as α_1, α_2, α_3, and α_4, respectively, and the angle variations generated by the rotation of each segment were φ_1, φ_2, φ_3, and φ_4, respectively; the counterclockwise rotation of the segment was considered positive. Figure 8 shows the coordinate system used in the correction process.

When a segment rotates around one end, the coordinate of the other end changes correspondingly, as shown in Figure 9. According to this geometric relationship, the variation of Y-coordinate can be given by

$$\Delta y = l\sin(\alpha+\varphi) - l\sin\alpha = l\sin\alpha\cos\varphi + l\cos\alpha\sin\varphi - l\sin\alpha. \tag{11}$$

As the segmental rotation angle is small, $\sin\varphi \approx \varphi$ and $\cos\varphi \approx 1 - \varphi^2/2$, giving

$$\Delta y = l\sin\alpha\left(1 - \frac{\varphi^2}{2}\right) + l\varphi\cos\alpha - l\sin\alpha \approx l\varphi\cos\alpha. \tag{12}$$

Similarly, the variation of X-coordinate is given by

$$\Delta x = l\cos(\alpha+\varphi) - l\cos\alpha \approx -l\varphi\sin\alpha, \tag{13}$$

where Δx and Δy are the variations of the X-coordinate and Y-coordinate (mm), respectively, l is the line distance between the joint rotation centers at both ends of a segment (mm), α is the angle between the segment and the positive direction of the X-axis (°), and φ is the segmental rotation angle (rad).

According to assumption (2), the coordinates of joints 1 and 6 remain unchanged, whereas the coordinates of joints 2–5 change because of segmental rotation.

The coordinate variations of joints 3 and 4 are, respectively, given by

$$\begin{cases} \Delta x_3 = -l_{OA}\varphi_1\sin\alpha_1 - l_{AB}\varphi_2\sin\alpha_2, \\ \Delta y_3 = l_{OA}\varphi_1\cos\alpha_1 + l_{AB}\varphi_2\cos\alpha_2, \end{cases} \tag{14}$$

$$\begin{cases} \Delta x_4 = -l_{CD}\varphi_3\sin\alpha_3 - l_{DE}\varphi_4\sin\alpha_4, \\ \Delta y_4 = l_{CD}\varphi_3\cos\alpha_3 + l_{DE}\varphi_4\cos\alpha_4. \end{cases} \tag{15}$$

Based on the principle that the length of the top block before and after deformation remains unchanged, the correction angle of each segment is

$$\beta = \frac{\sqrt{(x_4' - x_3')^2 + (y_4' - y_3')^2} - \sqrt{(x_4 - x_3)^2 + (y_4 - y_3)^2}}{l_{OB} + l_{CE}}, \tag{16}$$

where x_3' and x_4' are the X-coordinates of points B and C, respectively, after segmental rotation; y_3' and y_4' are the Y-coordinates of points B and C, respectively, after segmental rotation; and β is the modification of the rotation angle of each segment (rad).

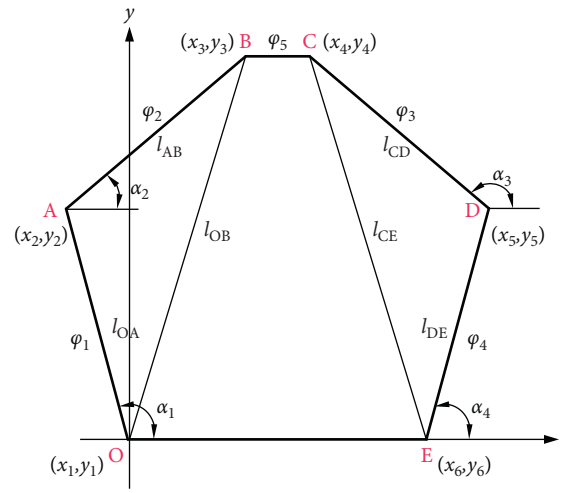

Figure 8: Coordinate system used in the derivation. Points O, A, B, C, D, and E are the rotation centers of each joint, not the middle points of the joints.

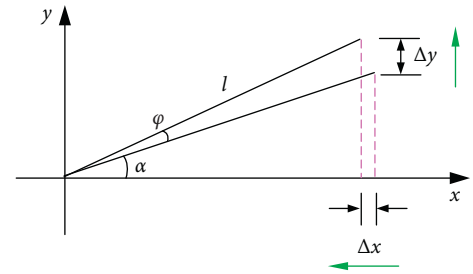

Figure 9: Relationship between segmental rotation and the coordinates of the joint.

The segmental rotation angle after modification can be expressed by

$$\varphi_1' = \varphi_1 - \beta, \tag{17}$$

$$\varphi_2' = \varphi_2 - \beta, \tag{18}$$

$$\varphi_3' = \varphi_3 + \beta, \tag{19}$$

$$\varphi_4' = \varphi_4 + \beta, \tag{20}$$

where $\varphi_1' - \varphi_4'$ are the segmental rotation angles after modification (rad).

By substituting the calculated values of Equations (17)–(20) into Equations (14) and (15), the corrected coordinate variation of points B and C can be obtained. Then, the rotation angle of the top block can be calculated as

$$\varphi_5 = \sin^{-1}\frac{y_4'' - y_3''}{\sqrt{(x_4'' - x_3'')^2 + (y_4'' - y_3'')^2}}, \tag{21}$$

where x_3'' and x_4'' are the X-coordinates of points B and C, respectively, after modifying the segmental rotations; y_3'' and y_4'' are the Y-coordinates of points B and C, respectively,

after modifying the segmental rotation angles; and φ_5 is the rotation angle of the top block (rad).

The joint opening angles of longitudinal joints 1–6 can be calculated as follows (a positive value indicates opening inwards; a negative value indicates opening outwards):

$$\theta_1 = \varphi_1', \tag{22}$$

$$\theta_2 = -\varphi_1' + \varphi_2', \tag{23}$$

$$\theta_3 = -\varphi_2' + \varphi_5', \tag{24}$$

$$\theta_4 = \varphi_3' - \varphi_5', \tag{25}$$

$$\theta_5 = -\varphi_3' + \varphi_4', \tag{26}$$

$$\theta_6 = -\varphi_4'. \tag{27}$$

By substituting the joint opening angles calculated by Equations (22)–(27) into equations (3), (6)–(9), the maximum joint opening width, horizontal diameter convergence, and bolt strain can be obtained. The correction process can be carried out multiple times to improve accuracy.

3.5. Early Warning Strategy. In a metro shield tunnel, the joint opening is generally required to be no more than 6 mm, in addition to the horizontal diameter convergence, less than 5‰ of D (where D is the outer diameter of the lining ring), and the bolt stress, less than the yield strength f_b. According to these three regulations, the limit values corresponding to the joint opening angle can be calculated when the joint is opened inwards and outwards, as shown in Table 1. The most unfavorable situation of horizontal diameter convergence was adopted as an example: two standard blocks increasing or decreasing simultaneously; that is, the joints on both sides of the bottom block open inwards or outwards at the same time. In addition, the design value of the yield strength of a grade of 6.8 bolts, that is, $f_b = 480$ MPa, was used as the yield stress limit of the bolt in Table 1.

4. Case Study

4.1. Site Description. The on-site application was conducted in a 500 m section of the down line between West Nanjing Road and the Natural Museum Station of Shanghai Railway Transportation Line 13. During the trial operation, this section was characterized by the nearby excavation of a large foundation pit. The relative plane and section location relationships between the pit and the tunnel are shown in Figures 10 and 11, respectively. The total excavation area of the foundation pit was about 4830 m^2, and the net distance between the excavation surface of the foundation pit and the top of the tunnel was about 9.8 m. The soil characteristics are listed in Table 2. The high density of buildings in this area made it necessary to monitor the deformation of the tunnels. To ensure the safety of the operation of this tunnel, a real-time monitoring system based on Internet of Things (IoT) was implemented. The monitoring system is comprised of three layers: a sensing layer, data transmission layer, and data analysis layer, as shown in Figure 12.

4.2. Sensor Installation. An inclinometer chip (SCA103T-D04 differential inclinometer) was used in the monitoring system to sense the rotation of the lining segments. This chip has the characteristics of high precision and good stability. Its measurement range is ±15° and measurement accuracy is 0.001°. The chip module, ZigBee module, and battery module are waterproof sealed to form a sensor module. The ZigBee module was used for data transmission, and the battery module supplied power for the inclinometer module. The user can adjust the acquisition frequency of the acquisition terminal. When the acquisition frequency is once a day, it is estimated that the battery pack can last one year.

Based on the assumption of rigid body segments, there is no theoretical difference in the installation position of the inclinometer module on a segment; however, some factors still need to be considered in the actual installation:

(1) The inclinometer module should not be too close to the joint position.

(2) The interval between the monitoring ring under the foundation pit and near the station should be reduced, and, accordingly, four sensors (as shown in Figure 13(a)) were arranged on each ring.

(3) It is necessary to consider the cost of the monitoring system, that is, to achieve a comprehensive understanding of the tunnel deformation by using as few sensors as possible.

(4) In the less important monitoring areas, only two sensors (P1 and P3 positions in Figure 13(a)) were arranged on each ring, and the deformation of the lining ring is assumed to be symmetrical about its vertical axis.

Finally, the schematic layout of the inclinometer modules was determined as shown in Figure 13(b). The monitored section contained 398 rings in total, 77 of which were installed with inclinometers for this study, including 34 cross sections (Section A) with four inclinometers installed in positions P1–P4 each and 43 cross sections (Section B) with two inclinometers installed in positions P1 and P3 each.

The installation of inclinometer modules on lining segments can be divided into the following steps:

(1) Determine the drilling position in advance on the design drawing of the lining ring according to the reinforcement position.

(2) Locate the predetermined drilling position on site using a steel tape.

(3) Use an impact drill to make two holes with a depth of 80 mm on the lining segment, with a diameter of 8 mm, as shown in Figure 14(a). After cleaning the dust in the hole, use the glue gun to fill the hole with glue, and then implant the chemical bolt with 8 mm diameter, as shown in Figure 14(b).

Table 1: Limits of the joint opening angle.

Evaluating indicator	Joint opening inwards	Joint opening outwards
Maximum joint opening width (mm)	$\Delta = (h - y)\theta = (350 - 115)\theta = 235\theta \le 6$ $\theta \le 0.0255$ rad	$\Delta = (h - y)\theta = (350–75)\theta = 275\theta \le 6$ $\theta \le 0.0218$ rad
Horizontal diameter convergence (mm)	$\Delta D = 2342(\theta_1 - \theta_4)\ \sin 71^\circ \le 31$ $\theta_1 - \theta_4 \le 0.0140$ rad	$\Delta D = 2269(\theta_1 - \theta_4)\ \sin 67^\circ \le 31$ $\theta_1 - \theta_4 \le 0.0148$ rad
Bolt stress (MPa)	$\Delta_b = \theta(h_{bt} - y) = 115\theta\sigma_b \le f_b = 480$ $\theta \le 0.0112$ rad	$\Delta_b = \theta(h_{bb} - y) = 45\theta\sigma_b \le f_b = 480$ $\theta \le 0.0287$ rad

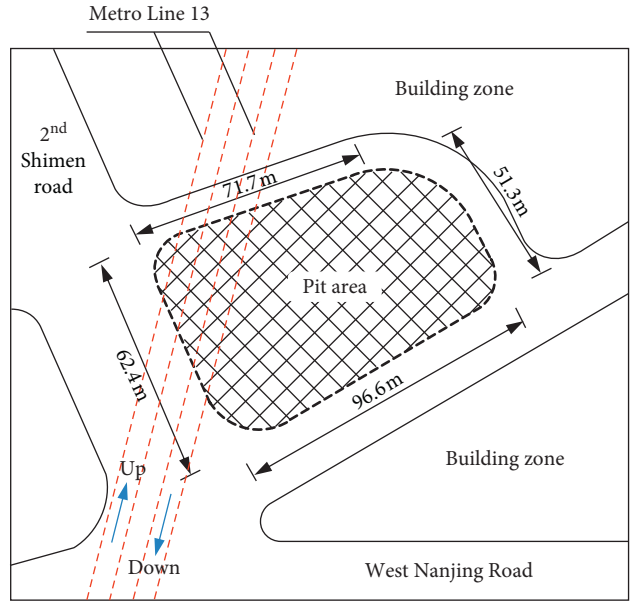

Figure 10: Relative plane location between the pit and the tunnel.

(4) Wait for two days after the implantation of the chemical bolts and then fix the inclinometer modules in place and tighten the nut to ensure firm fixation, as shown in Figure 14(c).

4.3. Data Transmission. The data transmission layer connected the data acquisition layer and the data processing and application layer. This layer used the ZigBee wireless network to transmit the field measurement data to the database. Three kinds of ZigBee modules were installed in inclinometer modules: (1) terminal nodes, which only send monitoring data but do not accept data; (2) routing nodes, which can accept or send data, play a role in routing, and can also assign addresses to nodes that join later; and (3) a network coordinator, also known as the central node, which is used to create a ZigBee network and assign an address to the node that originally joins the network. A ZigBee network needs only one central node, which is usually installed near the subway station. The central node sent the monitoring data to the general packet radio service (GPRS) data transmission terminal and then accessed the database through the GPRS signal. Figure 12 shows the schematic of the data transmission.

4.4. Comparison with Manual Data. The data analysis mainly includes the following steps: (1) modify the monitoring data and determine the opening direction of each joint; (2) calculate the joint opening angle, maximum joint opening width, horizontal diameter convergence, and bolt strain or stress by using the equations derived in the section entitled "Monitoring Method"; and (3) judge the state of the lining ring according to the early warning strategy.

To analyze the monitoring data comprehensively, the horizontal diameter convergences calculated by taking different positions of the joint rotation center were compared with those measured by the total station manually.

Taking Rings Nos. 257 and 289 as examples, the variation of the tunnel's horizontal diameter from May 1 to June 6, 2016, is shown in Figures 15 and 16. Both rings were directly below the foundation pit. In the legend, "uncorrected rotation center" represents the calculation result when the rotation center of each joint was taken as the center of the joint, and "corrected rotation center" represents the calculation result when the rotation center was taken as recommended values from the experimental study. The monitoring frequency of the monitoring system was once a day, while manual monitoring was performed once a week. The data for the same day were compared.

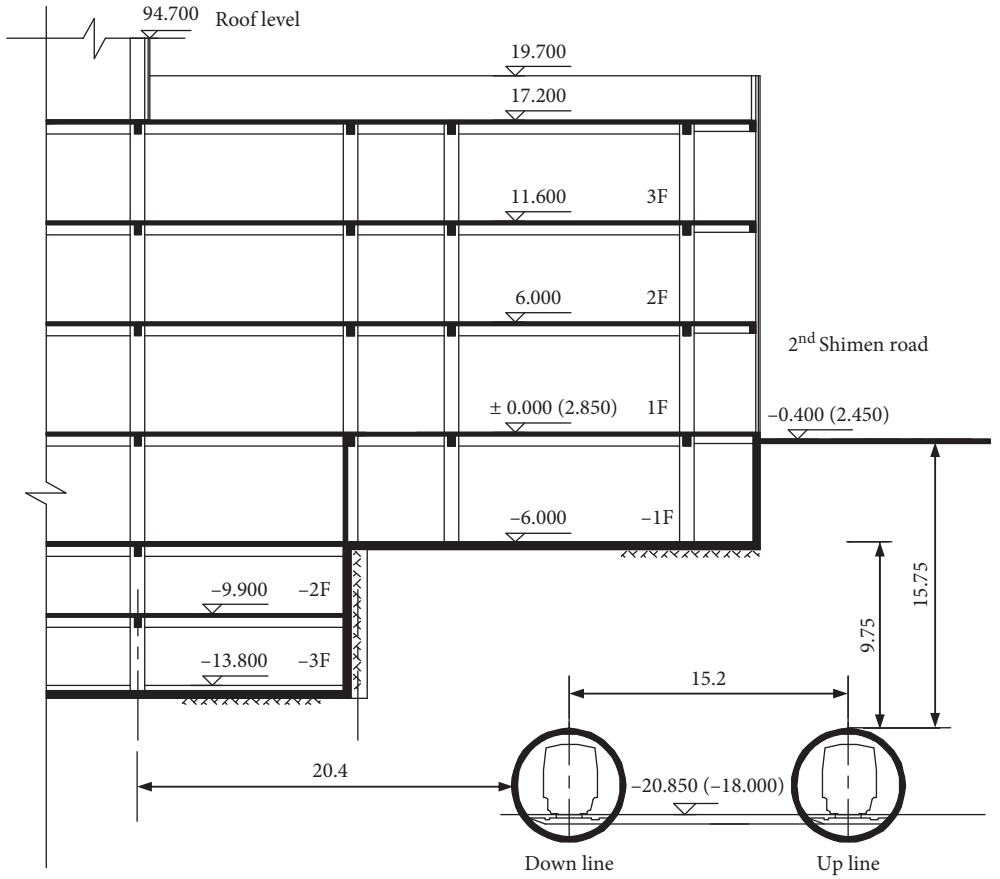

Figure 11: Section diagram between the pit and Shanghai Metro Line 13 (all distances are in m).

Table 2: Soil characteristics.

No.	Soil type	Thickness (m)	Weight (kN/m^3)	Static side pressure coefficient
1	Filling	1.55	19.0	—
2	Clay	1.7	18.3	0.49
3	Muddy silty clay	5.5	17.4	0.55
4	Muddy clay	5.8	16.5	0.58
5	Clay	1.7	17.6	0.51
6	Sandy silt	3.8	18.6	0.40
7	Clay	1.2	17.6	0.51
8	Silty clay	9.0	18.1	0.50

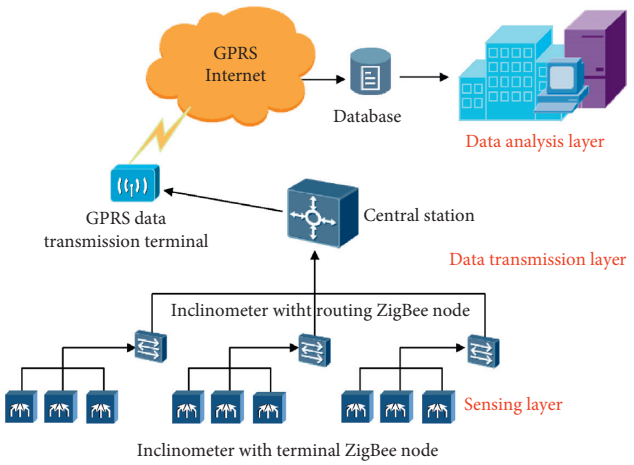

Figure 12: Schematic of the monitoring system network.

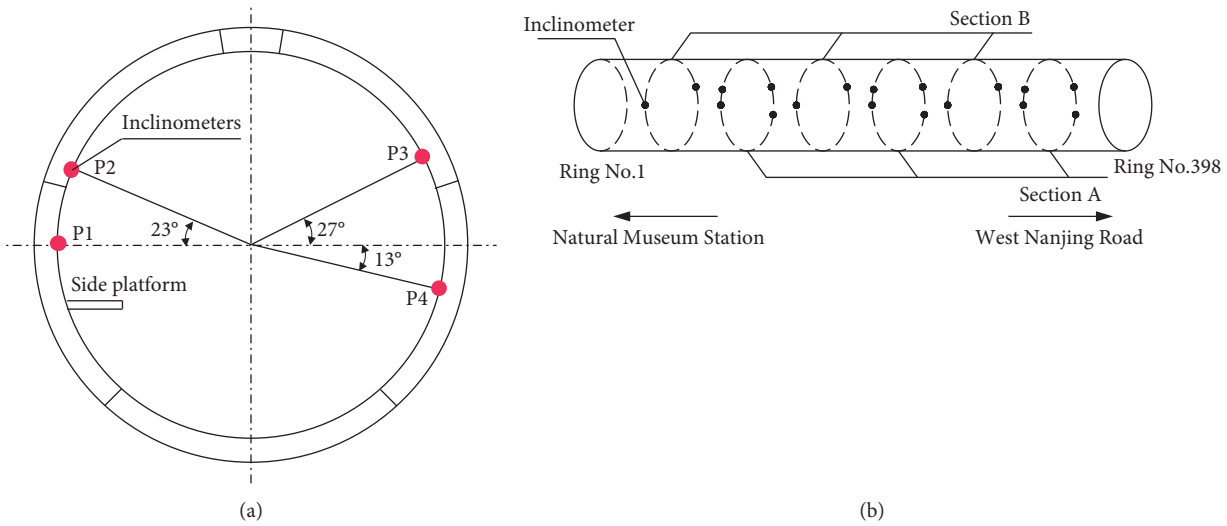

Figure 13: Sensor layout: (a) in a lining ring and (b) in the monitored section.

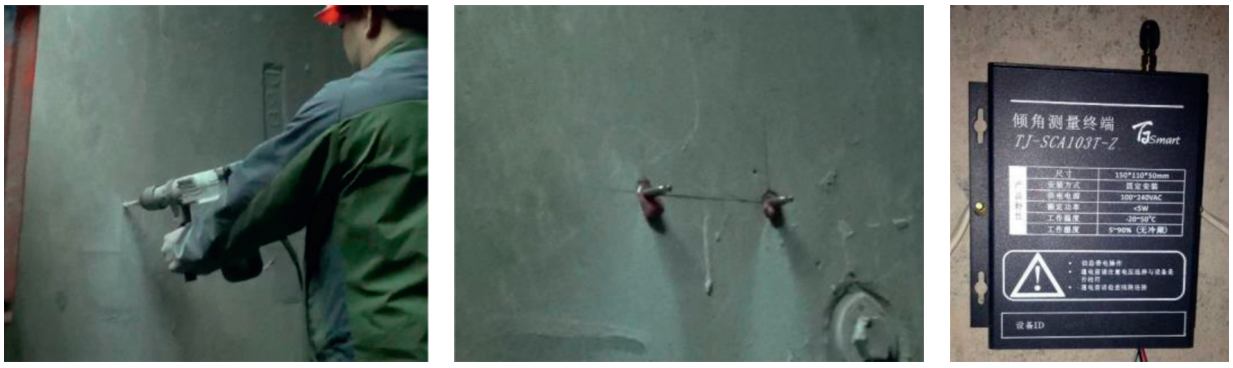

Figure 14: Installation process of inclinometer modules: (a) impact drilling, (b) insertion of the chemical bolts into the holes, and (c) fixing of the inclinometer modules.

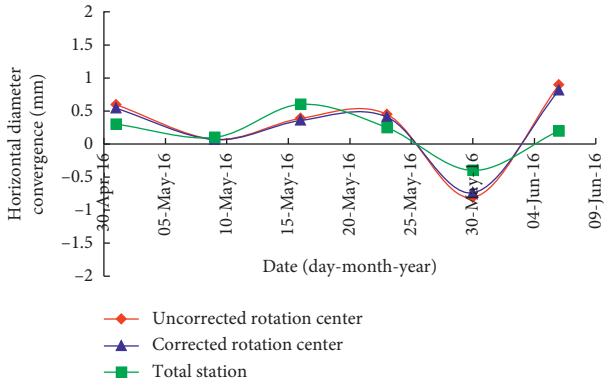

Figure 15: Variation of the tunnel's horizontal diameter for Ring No. 257.

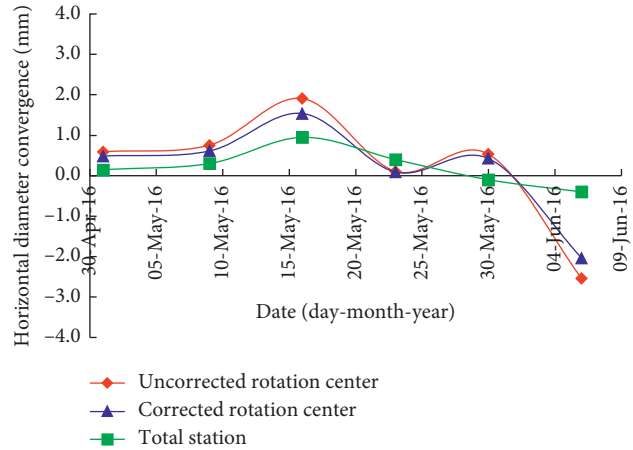

Figure 16: Variation of the tunnel's horizontal diameter for Ring No. 289.

As can be seen from the figures, when the recommended value of the joint rotation position was adopted, the calculation results were 8%–20% lower than those when the joint was located in the middle of the joint, further indicating the importance of considering the position of the joint rotation center. However, there are obvious differences between these two kinds of calculation results and the manual measurement results, which may be caused by the following factors:

(1) Because each inclinometer was fixed on the segment by two chemical bolts, some inclinometers may unavoidably not be fixed firmly, resulting in inaccurate data.

(2) The accuracy of the total station measurement is not particularly high, and the lining deformation is small, thus increasing the possibility of differences between the results.

5. Conclusions

Based on experimental research, equation derivation, and a case study, a method for monitoring the circular deformation of metro shield tunnels was systematically proposed. In general, the following conclusions were obtained:

(1) Through the experimental study, it was confirmed that the segment deformation showed rigid rotation under PBM and NBM conditions, and the recommended position of the joint rotation axis was 115 mm away from the compressive edge under PBM and 75 mm under NBM.

(2) Based on the rigid body and plane section assumption, the circular deformation monitoring method was derived. Through this method, the joint opening angle, maximum joint opening width, horizontal diameter convergence, and bolt strain were obtained using the rotation of segments.

(3) The monitoring error caused by the measurement error and the calculation model was corrected.

(4) A case study of the circular deformation monitoring system was implemented with data acquisition, data transmission, and data analysis functions.

(5) It was inferred that the position of the joint rotation axis had some influence on the accuracy of the calculation results, and the degree of influence was related to the deformation size of the lining ring.

(6) By using only inclinometers as sensors and incorporating IoT technology, the monitoring system established achieved the dual goals of automation and cost-effectiveness.

It is worth mentioning that a wireless system may not be as reliable and robust as a wired system and that the displacement of sensors themselves should be eliminated as much as possible. Further studies will focus on improving the effectiveness of the monitoring system and on applying it to diverse situations.

Data Availability

The data used to support the findings of this study are available from the corresponding author upon request.

Conflicts of Interest

The authors declare that there are no conflicts of interest regarding the publication of this paper.

Acknowledgments

The research was financially supported by the National Science and Technology Support Plan of China (Grant no. 2011BAK02B04).

References

[1] S.-M. Liao, J.-H. Liu, R.-L. Wang, and Z.-M. Li, "Shield tunneling and environment protection in Shanghai soft ground," *Tunnelling and Underground Space Technology*, vol. 24, no. 4, pp. 454–465, 2009.

[2] N.-A. Do, D. Dias, P. Oreste, and I. Djeran-Maigre, "2D numerical investigation of segmental tunnel lining behavior," *Tunnelling and Underground Space Technology*, vol. 37, pp. 115–127, 2013.

[3] A. Salemi, M. Esmaeili, and F. Sereshki, "Normal and shear resistance of longitudinal contact surfaces of segmental tunnel linings," *International Journal of Rock Mechanics and Mining Sciences*, vol. 77, pp. 328–338, 2015.

[4] B. Zhou, X. Xie, and Y. Li, "A structural health assessment method for shield tunnels based on torsional wave speed," *Science China Technological Sciences*, vol. 57, no. 6, pp. 1109–1120, 2014.

[5] J.-Y. Han, W. Zhao, P.-J. Jia, Y.-P. Guan, Y. Chen, and B.-F. Jiang, "Risk analysis of the opening of shield-tunnel circumferential joints induced by adjacent deep excavation," *Journal of Performance of Constructed Facilities*, vol. 32, no. 1, Article ID 04017123, 2018.

[6] C. Molins and O. Arnau, "Experimental and analytical study of the structural response of segmental tunnel linings based on an in situ loading test," *Tunnelling and Underground Space Technology*, vol. 26, no. 6, pp. 764–777, 2011.

[7] Y. Yuan, X. Jiang, and X. Liu, "Predictive maintenance of shield tunnels," *Tunnelling and Underground Space Technology*, vol. 38, pp. 69–86, 2013.

[8] Y. Yang, B. Zhou, X. Xie, and C. Liu, "Characteristics and causes of cracking and damage of shield tunnel segmented lining in construction stage-a case study in Shanghai soft soil," *European Journal of Environmental and Civil Engineering*, vol. 22, no. sup1, pp. s213–s227, 2018.

[9] P. Li, Y.-W. Zhang, F.-Y. Jiang, and H. Zheng, "Comprehensive health assessment of shield tunnel structure based on prototype experiment," *Journal of Central South University*, vol. 25, no. 3, pp. 681–689, 2018.

[10] T. Asakura and Y. Kojima, "Tunnel maintenance in Japan," *Tunnelling and Underground Space Technology*, vol. 18, no. 2-3, pp. 161–169, 2003.

[11] C. Shi, C. Cao, M. Lei, L. Peng, and H. Ai, "Effects of lateral unloading on the mechanical and deformation performance of shield tunnel segment joints," *Tunnelling and Underground Space Technology*, vol. 51, pp. 175–188, 2016.

[12] A. M. Zakhem and H. El Naggar, "Three-dimensional investigation of how newly constructed buildings supported on raft foundations affect pre-existing tunnels," *Transportation Geotechnics*, vol. 22, Article ID 100324, 2020.

[13] I. Ocak, "Interaction of longitudinal surface settlements for twin tunnels in shallow and soft soils: the case of Istanbul metro," *Environmental Earth Sciences*, vol. 69, no. 5, pp. 1673–1683, 2012.

[14] H. Chakeri and B. Ünver, "A new equation for estimating the maximum surface settlement above tunnels excavated in soft ground," *Environmental Earth Sciences*, vol. 71, no. 7, pp. 3195–3210, 2014.

[15] P. J. Bennett, Y. Kobayashi, K. Soga, and P. Wright, "Wireless sensor network for monitoring transport tunnels," *Proceedings of the Institution of Civil Engineers-Geotechnical Engineering*, vol. 163, no. 3, pp. 147–156, 2010.

[16] L. L. K. Cheung, K. Soga, P. J. Bennett, Y. Kobayashi, B. Amatya, and P. Wright, "Optical fibre strain measurement for tunnel lining monitoring," *Proceedings of the Institution of Civil Engineers-Geotechnical Engineering*, vol. 163, no. 3, pp. 119–130, 2010.

[17] S. Shen, Z. Wu, and M. Lin, "Distributed settlement and lateral displacement monitoring for shield tunnel based on an improved conjugated beam method," *Advances in Structural Engineering*, vol. 16, no. 8, pp. 1411–1425, 2013.

[18] Z. Z. Yin, "Application of hydrostatic leveling system in metro monitoring for construction deep excavation above shield tunnel," *Applied Mechanics and Materials*, vol. 333-335, pp. 1509–1513, 2013.

[19] J. Yin and H. Huang, "Real time monitoring method for the longitudinal settlement of shield tunnel using wireless inclinometer," in *Proceedings of the 2015 Information Technology and Mechatronics Engineering Conference (ITOEC 2015)*, Y. N. Chen and Z. Q. Zeng, Eds., pp. 274–280, Chongqing, China, March 2015.

[20] S. Bin and W. Xing, "The monitoring of segments dislocation deformation in shield tunnel based on BOFDA," *Engineering Challenges for Sustainable Underground Use, 1st GeoMEast International Congress and Exhibition on Sustainable Civil Infrastructures (EGYPT2018)*, S. Agaiby and P. Grasso, Eds., Springer, Berlin, Germany, pp. 222–232, 2017.

[21] H.-W. Huang, Q.-T. Li, and D.-M. Zhang, "Deep learning based image recognition for crack and leakage defects of metro shield tunnel," *Tunnelling and Underground Space Technology*, vol. 77, pp. 166–176, 2018.

[22] X. Wang, B. Shi, G. Wei, S.-E. Chen, H. Zhu, and T. Wang, "Monitoring the behavior of segment joints in a shield tunnel using distributed fiber optic sensors," *Structural Control and Health Monitoring*, vol. 25, no. 1, Article ID e2056, 2018.

[23] H. Huang, R. Xu, and W. Zhang, "Comparative performance test of an inclinometer wireless smart sensor prototype for subway tunnel," *International Journal of Architecture, Engineering and Construction*, vol. 2, no. 1, pp. 25–34.

[24] J. Zhang and M. Zhao, "A method to monitor the circular deformation of metro shield tunnels in soft soils," in *Proceedings of the 11th International Workshop on Structural Health Monitoring (IWSHM)*, F.-. Chang and F. Kopsaftopoulos, Eds.,pp. 1231–1238, Stanford, CA, USA, September 2017.